International Journal of Computer Information Systems and Industrial Management Applications
ISSN 2150-7988 Volume 18(7s) 2026 pp. 103-121
https://doi.org/10.70917/ijcisim-2026-3048
Article

HGSP-CNN: Hypergraph Spiking Neural Framework for Accurate Pulmonary Disease Classification using Chest X-Ray Images

JannuSwetha Priyanka[1,2]*, Senguttuvan Thenmozhi[1]

[1]Department of Electronics and Communication Engineering,Dayananda Sagar College of Engineering, Bangalore, India
[2]Department of Electronics and Communication Engineering, Vardhaman College of Engineering, Hyderabad, India
* Corresponding author's Email: swethapriyanka1823@gmail.com

Abstract: Pulmonary disease encompasses a diverse range of conditions that affect the respiratory system, including the nerves and organs involved in breathing. These disorders disrupt normal gas exchange, designing inhalation and exhalation difficult. They range from mild and self-limiting illnesses, such as the common cold and catarrh, to severe and life-threatening conditions, like Viral Pneumonia (VP), Tuberculosis (TB), Bacterial Pneumonia (BP) and acute respiratory syndromes like coronavirus disease 2019 (COVID-19). However, it is challenging to detect early-stage pulmonary disease using Computed Tomography (CT) scans and Chest X-Ray (CXR) images because of the similarity of pulmonary abnormalities to surrounding structures, which results in inefficient detections. To overcome this problem, this research proposes the Hypergraph Spiking P system based Convolutional Neural Network (HGSP-CNN) approach for pulmonary disease classification. The proposed HGSP-CNN dynamically constructs feature-dependent hyperedges from intermediate CNN activations while enabling high-order spatial reasoning. The experimental discoveries illustrate that proposed HGSP-CNN approach reaches the optimal accuracy of 99.58% and 99.25% on CXR14 dataset and COVID19 Radiography datasets as compared to the existing methods like ResNet50-V2 and PulmoNet.

Keywords: Computed Tomography, Convolutional Neural Network, Hypergraph Spiking P system, Pneumonia, Pulmonary disease.

1. Introduction

Pulmonary disease is the group of respiratory disorders which causes the lungs as well as respiratory system [1]. The pneumonia, COVID-19 and Tuberculosis are the important global health concerns which needs considerable backing to combat. These health concerns are the significant prevalent pulmonary disease worldwide as well as accurate analysis is complex for an effective conduct [2][3]. The clinical analysis or medical diagnosis tools like Chest X-Ray, Magnetic Resonance Imaging (MRI), Computed Tomography (CT) scans and Ultrasound (US) are widely applied to diagnosis the thoracic diseases [4][5]. Nevertheless, the manual observation of CXR images is an inefficient procedure and their understanding is stimulating for the radiotherapists because of the large nature of chest X-rays. Hence, there is a requirement for faster as well as most precise testing approaches to allow the large testing [6]. The early diagnosis from CXRs for the pulmonary disease provides an important clinical opportunity and thus directing the individuals for prior interventions like smoking cessation programs as well as medical therapy [7][8]. But, the similarity among the various lung disease as well as variations into an individual disease make their precise identification as a challenging task. The conventional diagnostic approaches mostly suffered from the subjectivity as well as variability between the clinicians, resulted in inconsistent results [9][10].

Machine Learning (ML) and Deep Learning (DL) are most broadly used in various areas, including image processing and so on [11]. Nevertheless, the conventional ML approaches for image classification mostly depends on the hand-crafted features, which require various phases for the extraction [12][13]. In contrast, the DL approaches have the benefit of automatically learning and extraction of appropriate features from the data, bypassing the requirement for manual feature extraction phase [14]. The important benefit of DL in this context is the removal of large feature engineering procedure typically integrated through conventional ML approaches [15]. Because of the advanced availability of the large-scale datasets, diverse attempts have been deployed for an automatic identification of lung-based disease through CXR images [16][17]. Despite significant breakthroughs in DL approaches for medical diagnostics, promptly and accurately identification of lung disease remains a

challenging endeavour [18]. The COVID-19 pandemic emphasized the significance of promptly as well as precisely classify the diseases to maintain and control the outbreaks efficiently. It is important to rapidly determine the COVID-19 cases from other lung issues due to its rapid spread and different symptoms [19]. The Tuberculosis and pneumonia remain important health concerns, especially in resource constrained areas. The accurate and timely prediction of the disease is important for avoiding the misclassification and misdiagnosis and to prevent the healthcare systems from the being overwhelmed [20].

The usage of DL models for pulmonary disease classification provided better results but several challenges remain unsolved. Most of the existing models such as CNN and transfer learning-based approaches mainly focus on local feature extraction and treat all spatial regions independently. This mechanism limited their ability to model complex inter-regional dependencies present in chest X-ray images. Furthermore, the pulmonary diseases such as pneumonia, tuberculosis, and COVID-19 exhibit overlapping radiographic patterns which are difficult to discriminate with conventional architectures. In addition, the existing models are sensitive to noise, illumination variation and class imbalance, as it led to reduced robustness and generalization in real-clinical settings. Therefore, there is a ned for an advanced classification framework which can explicitly capture higher-order spatial relationships. Moreover, the model needs to enhance structure and maintain computational efficiency. The present study addresses these limitations with the following contributions. The important contributions of this research are as trails:

- An optimized multi-stage preprocessing pipeline is introduced, including RGB conversion, resizing, normalization, gamma correction, CLAHE, Wiener filtering, and channel reconstruction. This ensures consistent illumination, enhanced contrast, and reduced noise, which improve the visibility of pulmonary patterns and facilitate robust feature learning.
- A HGSP-CNN is proposed to model complex inter-feature relations through hypervertex, hyperedge, and hierarchical neuron layers. This design enhances high-order spatial reasoning, enabling accurate discrimination among multiple pulmonary disease types.
- Extensive experiments are conducted on CXR14 and COVID-19 Radiography datasets using multiple baseline architectures. Comparative, ablation, and complexity analyses confirm that the HGSP-CNN achieves better accuracy, reduced computational cost, and enhanced generalization capability.

The rest of the paper is decided as trails: Section 2 illustrates the related works. Section 3 presents the proposed methodology. Section 4 illustrates the results and discussion. Section 5 provides a conclusion.

2. Related works

ML and DL approaches are broadly utilized in cardiovascular disease (CAD). The lung disease diagnosis is concentrated by various researchers in the past. An analysis of the reviewed studies reveals that most authors have employed ML and DL techniques on X-ray images to achieve high correctness and effectiveness in disease prediction, thereby facilitating the development of reliable diagnostic systems.

Mezina and Burget [21] implemented the neural network approach for chest X-ray estimation, which comprised of binary phases: Initially, Inception architecture which modelled the global features and another one was an integration of Inception modulus as well as Vision Transformer (ViT) network for an estimation of local features. The particular loss function named Asymmetric Loss Function (ASL) was applied for the multilabel classification. Moreover, the authors were most concentrated only on the subgroup of 9 diseases from CXR14 dataset, which occurred as a consequence of COVID19.

Irtaza [22] considered the various pre-trained methods such as MobileNet, DenseNet, EfficientNet, InceptionV3, VGG-16 and Xception for the multi-label lung disease classification. The target to enhance an effectiveness of those methods through the experimentation by parameter optimization. The MobileNet generated the optimal outcomes as compared to other approaches. The Deep Convolutional Generative Adversarial Network (GAN) was implemented to generate the synthetic X-ray images which involved diverse pathologies already involves in the selected imbalanced dataset.

Shamrat [23] implemented the fine-tuned MobileNetV2 approach for the multiclass classification of lung disease. The CLAHE approach was employed in the preprocessing step to enhance the image contrast. Moreover, the Gaussian Filter was employed for the noise removal from the images and data augmentation approaches were employed in the preprocessing step. The diverse Transfer Learning approaches like InceptionV3, AlexNet, DenseNet121, MobileNetv2 as well as VGG19 were considered for the classification process.

El-Magd[24] presented an explainable Artificial Intelligence (AI) framework for the identification and interpretation of chronic obstructive pulmonary disease (COPD) using exhaled breath sensor data. Five pre-trained CNNs were integrated with global average pooling and flattening layers for classification. a twin system based on

Case-Based Reasoning (CBR) was incorporated to enhance interpretability. However, the model was limited by a small sample size and restricted sensor diversity.

Abdulahi [25] developed a PulmoNet with a 26-layer CNN-assisted approach inspired through Wide Residual Network (WRN) architecture. The developed method involved the various layers and activation functions named ReLU and Softmax was utilized for multiclass classification. The model contained minimum training and detection time, designing it appropriate for real-time applications. The PulmoNet had the better capability to categorize the data into multiclass and detected the various pulmonary disease simultaneously. However, the PulmoNet was faced difficulty in handling complex disease patterns due to its fixed architecture and reliance on predefined features that affects the efficiency of the model.

Goyal and Singh [26] developed the Fusion approach of Recurrent Neural Network with Long Short-Term Memory (F-RNN-LSTM) for the detection and classification of lung disease through original X-ray images. The developed approach concentrated on the vigorousness as well as greater effectiveness through less computational efforts. The median filtering and histogram equalization approaches were considered in the preprocessing step. The dynamic region growing approach was employed for the extraction of Region of Interest (RoI) and the group of feature vectors had been developed through visual, texture, intensity and invariant moment features.

Bennour [27] presented the different DL approaches which were trained for the identification of the occurrence of particular lung diseases through thoracic radiography. An initial approach CovCXR-Net was used for the identification of binary class. The second approach MDCXR3-Net was used for the classification of input into three classes and the last approach MDCXR4-Net was used to the identify the input into four classes. Each model was personalized for particular classification issue it addressed and involved diverse architectural features which imitated to problem's nature.

Yi [28] implemented the unknown pulmonary disease diagnostic approach named BSD. Initially, three phases of bone suppression, extraction of pulmonary parenchyma as well as pulmonary disease diagnosis is encompassed. Next, aimed at the characteristics of chest X-ray image, a new segmentation approach named Improved U-Net was developed for the pulmonary extraction, in that, the actual convolutional layers of U-Net were modified through the novel designed function modules. Eventually, according to the characteristics of boneless pulmonary parenchyma, an improved function module RCA was employed for the feature extraction.

Even though, the above-mentioned existing models demonstrate promising performance in pulmonary disease classification, often struggle with several limitations. Firstly, the transfer learning and conventional CNN-based approaches primarily focuses on local features. These models lack mechanisms to explicitly model high-order spatial and relational dependencies among lung regions. Next, the graph-based and ensemble models improve feature representation but often rely on fixed architectures and predefined connection. This limited the model's ability to adapt complex pathological patterns. These limitations highlighted a need for novel framework which integrates relational reasoning, hierarchical feature modeling and reliable disease classification.

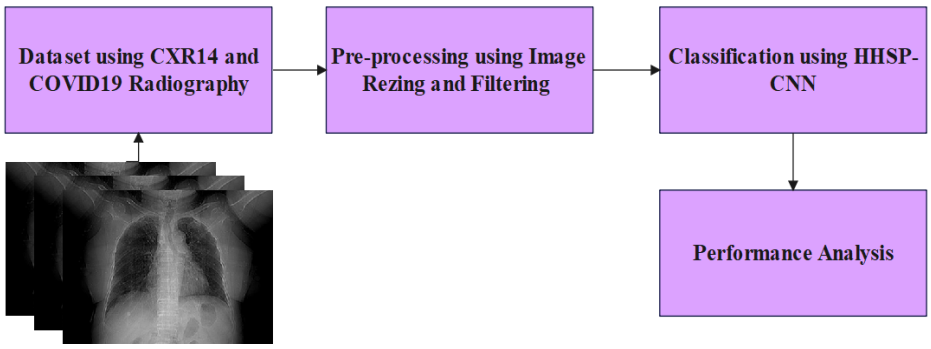

Figure. 1 Block diagram of proposed approach for pulmonary disease classification by HGSP-CNN

2.1 Problem Statement and Objective

The accurate detection of pulmonary disease like pneumonia, tuberculosis, and COVID-19 remains challenging due to the overlapping radiographic features among different disease types and normal cases. Traditional diagnostic practices depend on physical interpretation, time-intensive and disposed to observer variability. Although DL approaches have illustrated promising performance, their capability to capture large inter-regional dependencies within chest X-rays remains limited. Hence, this research designs a preprocessing pipeline that enhances image clarity, suppresses noise, and emphasizes pulmonary structures for improved feature

extraction by developing the Hypergraph Spiking P system-based CNN (HGSP-CNN) capable of learning hierarchical inter-feature relationships.

2.2. Research Gap

Despite the advancement in DL approaches for pulmonary disease detection, it is clearly showing that existing models heavily relied on conventional CNN or transfer learning architectures. The usage of these architectures failed to capture complex inter-regional dependencies. While few models like graph-based and ensemble model tried to enhance feature relationships often employed fixed connectivity structures also lack hierarchical reasoning. Additionally, majority of existing models are sensitive to noise, contrast variations and overlapping disease patterns which are commonly observed in chest X-ray images. These challenges limit the model's interpretability, robustness. to address these gaps, this research proposes aHypergraph Spiking P system-based CNN which models high-order spatial relationships through hypergraph structures and spiking neuron dynamics for robust disease classification.

3. Proposed Methodology

The proposed methodology introduces an intelligent hybrid learning framework named Hypergraph Spiking P system-based Convolutional Neural Network (HGSP-CNN) for classification of pulmonary disease from CXR images. The proposed HGSP-CNN model uses a ResNet-50 backbone pretrained on ImageNet. The network is truncated after the $Conv5_x$ block which produces a feature tensor of size $7 \times 7 \times 2048$ for an input resolution prior of 224×224. No global pooling is applied prior to the hypergraph processing. Each spatial location in the feature map is treated as a node in the subsequent hypergraph module. The output of this module is fed into a three-layer SPS followed by a fully connected classification layer with softmax activation. All the architectural components and dimensions remained fixed across datasets. Moreover, it integrates advanced preprocessing, hierarchical hypergraph representation, and spiking neuron modeling to capture high-order spatial dependencies among lung structures. This design enables precise detection of subtle abnormalities while maintaining computational efficiency. Fig. 1 illustrates the block diagram of proposed approach for pulmonary disease classification by HGSP-CNN.

3.1 Dataset Description

This research considers the two different dataset such as CXR14 [29] and COVID-19 Radiography dataset [30] to validate the effectiveness of proposed method. The datasets details are described in detail as.

3.1.1. CXR14 dataset

The ChestX-ray14 dataset is the greatest gatherings of anterior-perspective pulmonary X-ray scan data. The total of 112,120 bilateral thoracic X-ray data is acquired from the dataset in this research. This dataset totally involves 14 disease classes from 30805 individual patients. Although the CXR14 dataset originally contains 14 multi-label disease categories, it was simplified into five clear and clinically relevant classes: COVID-19, Bacterial Pneumonia, Viral Pneumonia, Tuberculosis, and Normal. But the chestX-ray14 dataset does not contain COVID-19 annotations in its original labelling.

Therefore, in this study, CXR14 is strictly used for non-COVID pulmonary conditions including Bacterial Pneumonia, Viral Pneumonia, Tuberculosis, and Normal cases. No COVID-19 labels are introduced into the CXR14 dataset. Moreover, any prior references to COVID-19 within the ChestX-ray14 context have been removed to avoid label ambiguity, phenotype leakage or unverifiable class assignments. All COVID-19 classification experiments are conducted exclusively using COVID-19 radiography dataset which includes verified COVID-19 annotations. This separation ensures label fidelity, avoids phenotype leakage and preserves clinical validity of the evaluation. Multi-label images were mapped to a single class using a priority rule, and ambiguous cases with overlapping target diseases were removed to avoid label noise. Images without any selected pathology were assigned to the Normal class, resulting in a clean and reliable multiclass dataset for training the proposed model.

3.1.2. COVID-19 Radiography dataset

COVID-19 Radiography dataset is widely performed in previous researches which concentrating on pneumonia as well as diverse infectious diseases. This dataset involves 1345 samples of pneumonia-afflicted samples and 1341 occurrences of CXR from patients through absence of visible health issues.

3.2 Preprocessing

The pre-processing illustrates the group of tasks applied to raw images to prepare them for next process. An aim of image preprocessing is to improve the important data from the image while preventing noise, artifacts, or

other undesirable characteristics which delay through pursuing analysis. The preprocessing phase significantly involves a series of operations like image resizing, color correction, scaling, filtering, noise reduction and image enhancement. These operations are selected according to on the characteristics of the images and the particular application requirements.

In this research, a multi-step preprocessing framework is employed for improving an excellence as well as and consistency of CXR images prior to classification. Initially, if an image is grayscale, it is converted into a three-channel RGB format by replicating the single channel to ensure compatibility with pretrained CNN models such as ResNet18, VGG19, MobileNetV2, InceptionV3, and the proposed HGSP-CNN. All images are resized to 224×224 pixels for keeping uniformity across datasets [31]. Subsequently, normalization scales pixel values in a range between 0 and 1, stabilizing training and accelerating meeting. Gamma correction ($\gamma = 1.2$) is then applied to improve contrast and correct illumination variations.

The RGB image is temporarily converted to grayscale for enhancement operations, where Contrast Limited Adaptive Histogram Equalization (CLAHE) is applied to highlight fine pulmonary textures, opacities, and nodules in low-contrast regions. To further enhance image clarity, Wiener filtering with a 3×3 window is employed to remove random noise and retain subtle structural details. After enhancement, the grayscale image is reconstructed into three identical RGB channels to maintain model compatibility, followed by conversion to 8-bit integer format (0–255 range) for efficient storage and processing. This preprocessing sequence ensures superior feature quality and optimized learning performance for the HGSP-CNN model.

To ensure true generalization and avoid data leakage, the dataset was split strictly at the patient level, preventing any patient's images from appearing in both training and testing sets. All preprocessing settings, including normalization, CLAHE, and gamma correction, were computed only from the training data and applied unchanged to the test set. Data augmentation was used exclusively on training images, while all metadata that could reveal patient information was removed. Fixed random seeds ensured reproducibility, and the final test evaluation was done only once. These steps guarantee that the reported accuracy is free from any near-perfect separability.

Furthermore, for the datasets containing overlapping pulmonary annotations, a deterministic and auditable label harmonization procedure was applied. Each image was assigned with a single target label only if exactly one disease category matched the predefined class definitions. The images exhibiting multiple target disease annotations were excluded to prevent phenotype leakage. No priority-based reassignment was performed. All the inclusions and exclusion rules were predefined and verified against the original dataset label metadata. After the successful filtering and preprocessing the updated samples on datasets is given in below Table 1 & 2.

Table 1. Total available input samples from CXR14 after preprocessing

Class	**Final Samples Used**	**Training (80%)**	**Testing (20%)**
Bacterial Pneumonia	8,950	7,160	1,790
Viral Pneumonia	8,620	6,896	1,724
Tuberculosis	5,430	4,344	1,086
Normal	78,120	62,496	15,624
Total	101,120	80,896	20,224

Table 2. Total available input samples from COVID-19 Radiography Dataset after preprocessing

Class	**Final Samples Used**	**Training (80%)**	**Testing (20%)**
COVID-19	460	368	92
Pneumonia	445	356	89
Normal	440	352	88
Total	1,345	1,076	269

Table 1 and 2 presents the exact number of samples per class after deterministic label harmonization and preprocessing for CXR14 and COVID-19 datasets. In CXR14 dataset, multi-label images containing overlapping

pulmonary conditions were excluded to prevent the phenotype leakage while resulting in 11000 removals. The final datasets were split with strict patient-wise separation using an 80:20 training and testing ratio.

3.3 Classification using HGSP-CNN

The proposed method trains a HGSP-CNN for pulmonary disease classification. Unlike traditional CNNs, this model integrates a hypergraph layer to capture higher-order relationships among image features, which helps in distinguishing subtle and overlapping disease patterns. The proposed HGSP-CNN approach contains three layers:

- **Hypervertex Layer:** CNN backbone scans the X-ray and identifies basic local features like edges, textures, and small patterns from every part of the image. Each of these features becomes a "hypervertex".
- **Hyperedge Layer:** This is where the model starts to reason. The hypergraph groups individual features (hypervertices) into larger, medically meaningful patterns, known as "hyperedges".
- **Hyper-upper Layer:** At this final level, the model combines the evidence from the pattern groups (hyperedges) to identify the specific disease.

CNN is a multi-layer perceptron NN, employed for various fields such as image processing, object detection and so on. CNN has the better capability to extract the image features and classify them into multiclass. The CNN architecture comprised of various layers such as convolution, pooling, and dense [32]. After the extraction of features, a hyperedge construction mechanism is included. The hyperedges are constructed from intermediate CNN feature maps to capture high-order spatial relationships among salient regions. Particularly, the feature maps extracted from the final convolutional layers are partitioned into non-overlapping spatial regions where each treated as a node in hypergraph. For each node, a mean activation across channels is computed. The node exhibiting activation values above predefined threshold τ are grouped to form a hyperedge. This formation enables the modeling of multi-region dependencies. The incidence matrix is therefore sparse with node-hyperedge associations determined by activation strength. This effective formulation of hyperedges allows the hypergraph to adapt dynamically to discriminative feature responses while maintaining computational efficiency. The Spiking P Systems (SPS) employs better in diverse applications, however, traditional (SPS) are 2D graph structures, where neurons transmit in plane, preventing that actual neurons connect, hierarchical as well as transmembrane, constraining their model understanding capability of (SPS). A hypergraph is a flexible topological structure which defines the large hierarchical as well as greater-order dealings. Hence, to address the previously discussed problem, this research introduces the hypergraphs in SPS for employing the large hierarchical estimations, keep intermediate outcomes as well as define greater-orders relations.Assume that CNN feature map is denoted as $F \in \mathbb{R}^{H\times W\times C}$ and each spatial location (i, j) defines node v_k. Node activation a_k is computed as the mean value across all C channels. The hyperedges are formed by grouping nodes whose activation exceeds a threshold τ are defined as 75th percentile of activations computed on training set. The resulting incidence matrix $H \in \{0,1\}^\{N \times E\}$ is sparse with each node assigned to at most one hyperedge per iteration. This deterministic procedure prevents phenotype leakage. Moreover, for each input image, the truncated CNN backbone produces a feature map of fixed spatial resolution $H \times W \times C$. Each spatial location in this feature map is considered as the hypervertex that results in a fixed number of hypervertices per image which is equal to $H \times W$.

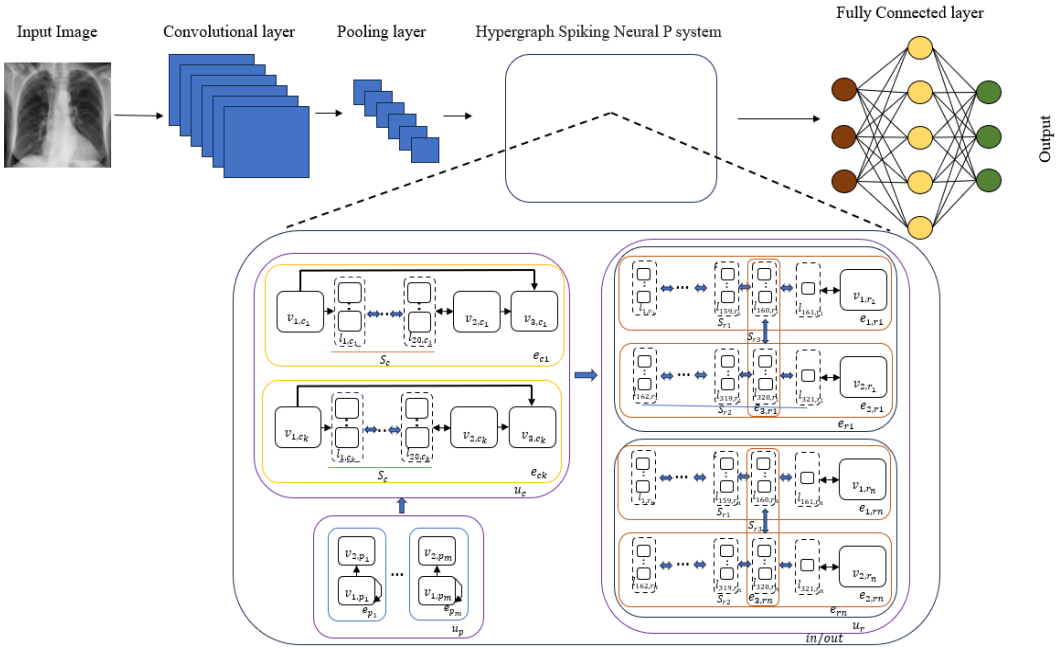

Figure. 2 The systematic architecture of HGSP used for pulmonary disease classification

As the CNN model used the output resolution of 7×7 which yields 49 hypervertices for every image. In addition, these hyperedges are constructed dynamically based on activation statistics. For each hypervertex, the mean activation across all the channels is computed and a global threshold is defined as the 75 th percentile of activation values. The hypervertices exceeding this threshold value are grouped into a spatially connected cluster and formed as one hyperedge. Consequently, the number of hyperedges per image is not fixed and it mainly depends on the activation depends on activation distribution of that specific sample. Images with extensive pathological regions generate more activated clusters which produces higher number of hyperedges. Similarly, the normal images typically produce fewer hyperedges. Therefore, the number of hyperedges ranged between 4 and 9 per image across the dataset. This adaptive mechanism ensures that the hypergraph structure reflect image-specific structural complexity instead of imposing the static connectivity pattern. For an input image of size $224 \times 224 \times 3$, the ResNet-50 model produced an output tensor with a spatial resolution of 7×7 with 2048 channels. Therefore, the exact feature dimension per image is considered as $7 \times 7 \times 2048$. Each of the 7×7 spatial locations are treated as the hypervertex that resulted in 49 hypervertices per image. The 2048-dimesional channel vectors at each spatial location represents the local deep feature descriptor used for the activation computation and hyperedge construction. Considering that the hypergraph $G = (V, E)$, V means a finite vertex set of G, and every graph is known as hypervertex.

E describes a hyperedge group of G, which is illustrated through developing the vertex-edge correlation matrix $H = (v, e)$ of $|V| \times |E|$ dimensions, which is formulated in Eq. (1) as follows:

$$H(v,e) = \begin{cases} 1 \; if \; v \in e \\ 0 \; if \; v \notin e \end{cases} (1)$$

Where, $H(v,e)$ illustrates the incidence function; v and e denotes the hypervertex and hyperedge respectively. According to this, various classes of neurons are acquired such that the hypervertex, hyperedge and hyper-upper. A general neuron layer is described as a group of hypervertex neurons. The hyperedge neuron is a neuron which involves various hypervertex neurons, which involves hyperedge neurons are inside and in/out neuron is outside. A neuron for inputting as well as outputting spikes is an in/out neuron. The systematic architecture of HGSP which worked for pulmonary disease classification is represented in Fig. 2.

As demonstrated in this Fig. 2, a hypergraph G involves the hypervertices $V = \{v_1, v_2, v_3, v_4, v_5, v_6, v_7, v_8, v_9, v_{10}, v_{11}\}$ and hyperedges $E = \{e_1, e_2, e_3\}$. e_1 involves $\{v_1, v_2, v_3, v_4\}$, e_2 involves $\{v_3, v_5\}$ and e_5 involves $\{v_5, v_6, v_7, v_8, v_9, v_{10}, v_{11}\}$, where, $\{v_1, v_2, v_3, v_4\}$, $\{v_3, v_5\}$ and $\{v_5, v_6, v_7, v_8, v_9, v_{10}, v_{11}\}$ are hypervertex neurons into hyperedge neurons e_1, e_2 and e_3 individually.

u_1 and in/out are hyper-upper neuron as well as input/output neuron individually. General neuron layers are l_1, l_2 and l_3 such as hypervertex neurons $\{v_6, v_7\}$, $\{v_8, v_9\}$ and $\{v_{10}, v_{11}\}$ individually. Influences among various general neuron layers l_1, l_2 as well as l_2, l_3 are described through graph structures S_1, S_2 between hypervertex neurons $\{v_6, v_7\}$, $\{v_8, v_9\}$ and $\{v_8, v_9\}$, $\{v_{10}, v_{11}\}$. Then, this research describes the HGSP of degree $m \geq 1$, is formulated in Eq. (2) as trails:

$$\Pi = (\varphi, \sigma_k, L, syn, in/out) \qquad (2)$$

Here,Π specifies the complete SPS approach; L denotes the set of rules that governs spiking, communication, and transformation of spike trains; syn means a synaptic connection structure;$\varphi = \{\alpha\}$ describes group of spikes α; $\sigma_k = \{\sigma_v, \sigma_e, \sigma_u\}$ denotes the group of neurons in HGSP, where, $k \in \{v, e, u\}$ denotes neuron classes; σ_v, σ_e and σ_u illustrates the group of group of hypervertex, hyperedge and hyper-upper neurons individually. The information of such hyper neurons is described as $\sigma_k = \{n_k, T_k, \omega_k, R_k\}$. The n_k denotes primary number of spikes in σ_k. $T_k = \{\tau_{k,1}, \ldots, T_{k,d}\}$ denotes spike train in σ_k. A metric k, d illustrates a length d of spike train T_k, ω_k is a weight of spike train and R_k illustrates finite group of guidelines through pursuing various forms.

- **Plane rules:** This is employed among the similar classes of merged neurons, is formulated in Eq. (3) as follows:

$$\left[\alpha^c, \omega_{k_i} T_{k_i} \rightarrow \alpha^p, \omega_{k_{i+1}} T_{k_{i+1}}\right]_{k_i} \qquad (3)$$

Where, α^c illustrates number of spikes consumed; ω_{k_i} and $\omega_{k_{i+1}}$ denotes the weight of the spike train currently present and next neuron k_i and k_{i+1} respectively. T_{k_i} is a spike train associated with neuron k_i; $T_{k_{i+1}}$ illustrates the updated spike train generated for the next neuron in the hierarchy or hyperedge connection. α^p means a number of spikes produced and sent to the next connected neuron after the rule fires.Neuron σ_{k_i} will utilize c count of spikes α and generate p count of α to its merged neuron $\sigma_{k_{i+1}}$. Simultaneously, a spike train T_{k_i} is changed to $T_{k_{i+1}}$ to $\sigma_{k_{i+1}}$ through its weight changed from ω_{k_i} to $\omega_{k_{i+1}}$. Moreover, the proposed model operates using plane, transmembrane and hierarchical rules to regulate spike propagation. The plane rules govern intra-membrane spike accumulations while the transmembrane rules control spike transmission between adjacent membranes. These hierarchical rules coordinate spike flow across multiple membrane levels. During each simulation step, the plane rules are applied parallelly followed by transmembrane communication. Finally, follows the hierarchical control updates and this deterministic update ordering ensures stable spike dynamics, consistent feature transmission across iterations.

- **Transmembrane rules:** Advantaging from hypergraph structure, a transmembrane communication is employed among the binary hypervertex neurons σ_{v_i} and $\sigma_{v_{i+1}}$, where, σ_{v_i} as well as $\sigma_{v_{i+1}}$ depends on minimum hyperedge neurons such as v_3 and v_5. The v_3 depends on the hyperedge neurons e_1 and e_2. The v_5 depends on the e_2 and e_3. The transmembrane communication is employed among v_3 and v_5 impacted through e_2, which is formulated in Eq. (4) as follows:

$$\left[\alpha^c, \omega_{v_i} T_{v_i} \rightarrow \alpha^p, \omega_{v_{i+1}} T_{v_{i+1}}\right]_{v_i} \qquad (4)$$

Neuron σ_{v_i} will utilize c count of spikes α and generate p count of α to its merged neuron $\sigma_{v_{i+1}}$. Simultaneously, the spike train T_{v_i} is changed to $T_{v_{i+1}}$ to $\sigma_{v_{i+1}}$ through its weight changed from ω_{v_i} to $\omega_{v_{i+1}}$.

- **Hierarchical neurons:** These rules are executed among merged neurons of hierarchical relationships, which is formulated in Eq. (5) as follows:

$$\left[\alpha^c, T_k \rightarrow \alpha^p T_q\right]_k \qquad (5)$$

Where, T_q illustrates the new spike train generated and transmitted to the next neuron q; q illustrates the index of target neuron receiving the output spike train from neuron k. Neuron σ_k will utilize c count of spikes α and generate p count of α to its merged neuron σ_q. Simultaneously, a spike train T_k is changed to T_q to σ_q. Moreover, the Hypergraph-guided Spiking P System consists of both trainable and fixed components. The trainable parameters include synaptic weight matrix W which governs spike transmission between hypervertices. The potential scaling parameters and final fully connected classification layer. The fixed components including hypergraph, spike threshold and spike reset mechanism. These structural and rule-based elements remain constant during training to preserve biologically inspired firing dynamics. Consequently, the firing threshold was initialized using training-set activation statistics and remained fixed during training. It was not updated through back propagation but only synaptic weights and classifier parameters were optimized. Algorithm 1 specifies the pseudocode of proposed approach for better reproducibility.

Algorithm 1: Pseudocode of HGSP-CNN for Pulmonary Disease Classification

Input: Chest X-ray image dataset D = {I_1, I_2, …, I_n}

Output: Predicted class labels C = {COVID-19, Pneumonia, TB, Normal}

1. Preprocessing Phase:

1.1 For each image I in dataset D:

Convert grayscale image to RGB (3-channel), resize I to 224 × 224 pixels, normalize pixel values in range [0, 1], apply Gamma Correction (γ = 1.2) to adjust illumination, convert to grayscale and apply CLAHE for contrast enhancement, apply Wiener filter (3×3) for noise suppression and reconstruct enhanced image back to RGB format.

1.2 Store the preprocessed image set as D_preprocessed.

2. Feature Extraction (CNN Backbone):

2.1 Feed D_preprocessed into CNN backbone (e.g., modified ResNet block).

2.2 Extract local spatial features $F = \{f_1, f_2, \ldots, f_m\}$.

2.3 Map each feature f_i to a hypervertex node v_i in the hypergraph.

3. Hypergraph Construction:

3.1 Define vertex set $V = \{v_1, v_2, \ldots, v_m\}$.

3.2 Define hyperedge set $E = \{e_1, e_2, \ldots, e_k\}$,

where each e_j connects multiple related features.

3.3 Construct incidence matrix $H(v, e)$ of dimensions $|V| \times |E|$.

3.4 Initialize neuron layers:

- Hypervertex Layer (L_v): Local feature neurons.
- Hyperedge Layer (L_e): Relational feature neurons.
- Hyper-upper Layer (L_u): Hierarchical reasoning neurons.

4. Spiking P System (SPS) Modeling:

4.1 For each neuron $n \in \{L\_v, L\_e, L\_u\}$:

- Initialize spike count $S_0(n)$ and threshold $\theta(n)$.

4.2 Apply plane communication rule:

$n_i (S_i) \rightarrow n_j (S_j)$ within same neuron class.

4.3 Apply transmembrane communication rule:

$n_i (S_i) \rightarrow n_j (S_j)$ across different neuron layers via hyperedges.

4.4 Apply hierarchical neuron rule:

Higher-level neuron aggregates spikes from lower layers.

5. Classification Phase:

5.1 Flatten final spiking activations from L_u.

5.2 Pass through fully connected (dense) layer.

5.3 Apply Softmax function for multiclass prediction:

$$\hat{y} = Softmax(W \cdot L\_u + b)$$

5.4 Assign class label $\hat{C}$ = argmax($\hat{y}$)

6. Training and Optimization:

6.1 Use cross-entropy loss

6.2 Update network weights using Adam optimizer.

6.3 Repeat until convergence or validation loss stabilizes.

7. Output:

Return predicted class labels $\hat{C}$ for all test images

4. Experimental Analysis

All experiments for the proposed method were conducted in MATLAB environment on a Windows 10 operating system with a16GB RAM and an Intel i5 processor. The training and testing portions of an obtained dataset were partitioned in a ratio of 80:20. To validate the significance of the proposed method, several key performance indices are considered. These hyperparameters are selected using Bayesian optimization that effectively explores the search space by modeling the performance objective as a probabilistic function. This optimization technique was performed over 40 trials to tune learning rate, batch size, weight decay, dropout and membrane scaling using validation F1-score as the objective. This strategy balances exploration and exploitation while enabling the identification of optimal configurations with fewer evaluation while ensuring stable convergence and reduced overfitting. The hyperparameter table is given in below Table 3.

Table 3. Defining the Hyperparameters with corresponding values

Hyperparameter	**Value**
Batch size	32
Number of epochs	80
Early stopping	F1-score
Learning rate	0.001
Optimizer	Adam
HGSP spiking cycles	12
Firing threshold	moderate

These settings consistently produced strong and reliable performance across all datasets. In addition, to prevent leakage and selection bias, no cross-dataset label inference was performed. The ambiguous samples were excluded only when the disease annotations overlapped target categories. The COVID-19 annotations are not presented in the dataset. The patient-wise separation was strictly performed and dataset mappings including exclusions rules were followed across all experiments to prevent subject overlap between training and evaluation sets. The data splits were generated using fixed random seeds and stratified to preserve class distribution across folds. No patient identifiers were shared across training, validation or the testing partitions. Also, the proposed model and baseline models are evaluated under same experimental scripts, fixed random seeds, dataset splits and preprocessing configurations in performance and ablation studies to support reproducibility and evaluation.

Accuracy represents the overall capability of the classifier to correctly categorize chest X-ray images, ensuring that healthy cases are recognized as healthy and those with lung disease are identified as diseased. Precision denotes an extent to which the model accurately detects lung disease cases without misclassifying healthy samples

as affected. Recall reflects the efficiency of the classifier in detecting all existing lung disease samples within the dataset. F1-score is the weighted average of precision and recall. The Receiver Operating Characteristic (ROC) curve is used to examine the capability, of a model, of distinguishing between classes and is plotted using measures named True Positive Rate (TPR) and False Positive Rate (FPR). The mathematical expressions of these metrices are formulated in Eqs. (6) to (10) as pursues:

$$Accuracy = \frac{TP+TN}{TP+TN+FP+FN} \quad (6)$$

$$Precision = \frac{TP}{TP+FP} \quad (7)$$

$$Sensitivity = \frac{TP}{TP+FN} \quad (8)$$

$$F1-score = 2 \times \frac{Precision \times Sensitivity}{Precision+Sensitivity} \quad (9)$$

$$Specificity = \frac{TN}{TN+FP} \quad (10)$$

Where TP, TN, FP and FN denote True Positive, True Negative, False Positive and False Negative, respectively. Moreover, the gradient propagation has been done through surrogate gradient to handle the non-differentiability of spiking events. During the forward pass, membrane potentials generate binary spikes based on fixed firing threshold. In the backward pass, a smooth surrogate function approximates the spike activation gradient and enables effective gradient flow via spiking neurons. The gradient propagates from the classification loss via the SPS layer, hypergraph module and CNN backbone. At last, the model optimization is performed using the Adam optimizer with fixed learning rates and batch sizes as described in the experimental configurations.

4.1 Performance Analysis

This section employs a comprehensive performance estimation of proposed HGSP-CNN method for pulmonary disease classification operations by using three standard datasets. This research employed the estimation mechanism utilized through different existing DL approaches to perform a comparative analysis of proposed approach with respect to existing methods studied in this research. The results obtained using k-fold validation and the reported values correspond to the average performance across all the fold. These results ensure robustness and reducing bias due to data partitioning. The evaluation confirms model's consistent generalization across all the classes. These results in this table including baseline models and proposed model are validated under the identical experimental settings described earlier with k-fold with patient-wise separation across folds. This strategy ensures label fidelity, prevents phenotype leakage and maintains the clinical validity and reproducibility of the reported performance.

Table 4 demonstrates that proposed HGSP-CNN significantly outperforms conventional CNN-based models such as VGG19, MobileNetV2, ResNet18, and InceptionV3. The inclusion of hypergraph connectivity enables an approach for modelling multi-level spatial dependencies and relational features among lung regions, resulting in notable improvements in accuracy (99.58% and 99.25%) and F1-score. The high specificity indicates approach's strong capability to correctly determine healthy cases, reducing false positives. Moreover, the statistical validation is included where the results evaluated with the help of mean and standard deviation across folds with 95% Confidence Interval (CI) estimated for each metric. A null hypothesis is included where it assumes no performance variation across folds which is tested using paired t-tests while confirming the statistical consistency.

Table 4. Performance analysis of proposed method with different classifiers

Dataset	Methods	Accuracy (%)	Precision (%)	Recall (%)	F1-score (%)	Specificity (%)	*p*-value
CXR14	VGG19	97.10	96.88	96.58	96.65	97.01	0.006

	MobileNetV2	96.45	95.96	95.75	95.88	96.87	0.004
	ResNet18	98.47	98.07	97.97	97.95	98.77	0.003
	InceptionV3	98.85	98.63	98.43	98.50	98.72	0.039
	Proposed	99.58	99.46	99.17	99.34	99.68	0.002
	VGG19	96.85	95.42	95.63	96.12	96.34	0.007
	MobileNetV2	97.42	96.28	96.51	97.03	97.11	0.005
	ResNet18	98.02	97.11	97.33	97.84	97.92	0.004
	InceptionV3	98.47	97.64	97.82	98.21	98.34	0.039
COVID-19	Proposed	99.25	98.23	98.43	99.37	99.21	0.001

Table 5. Computational complexity of proposed method with existing methods

Dataset	Methods	Run time memory (MB)	Computational time (s)	Instance time (ms)
CXR14	VGG19	15.75	190.98	4.5
	MobileNetV2	10.57	88.78	2.8
	ResNet18	8.76	120.76	2.7
	InceptionV3	8.93	140.67	3.2
	Proposed	5.87	112.89	2.3
COVID-19	VGG19	10.32	182.4	4.2
	MobileNetV2	9.56	95.7	2.1
	ResNet18	9.54	121.6	2.8
	InceptionV3	7.87	138.2	3.1
	Proposed	4.765	110.5	2.4

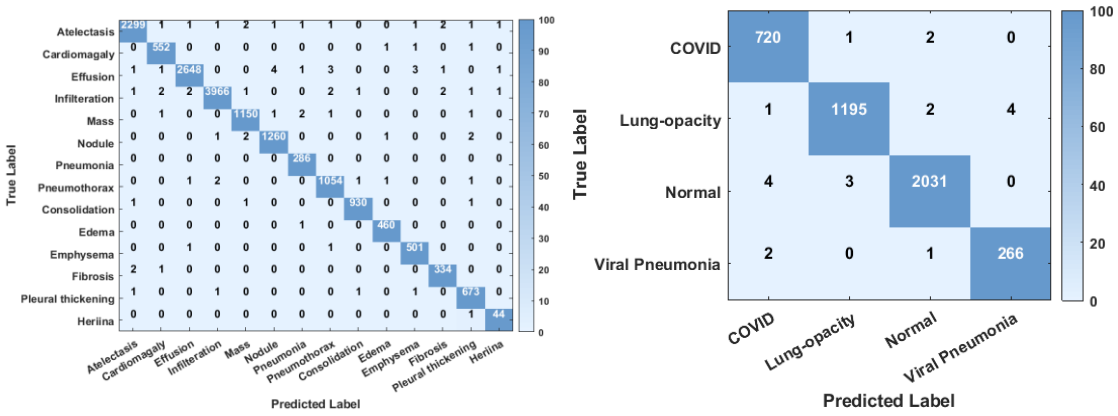

(a)(b)

Figure. 3 Confusion matrix of proposed method for pulmonary disease classification, (a). CXR14 dataset, (b). COVID-19 Radiography dataset

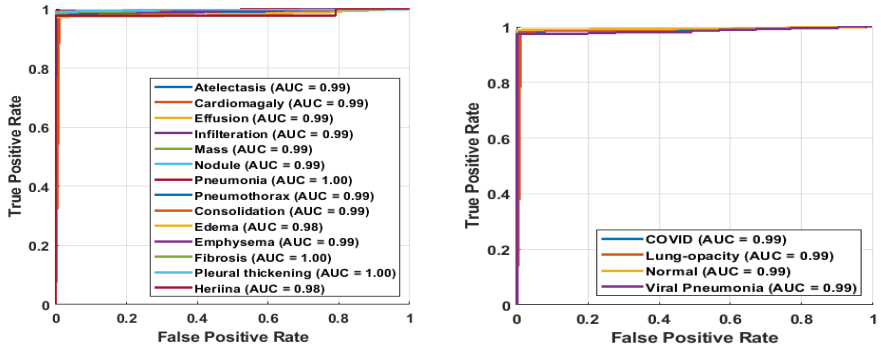

(a) (b)

Figure. 4 ROC curve of proposed method for pulmonary disease classification, (a). CXR14 dataset(b). COVID-19 Radiography dataset

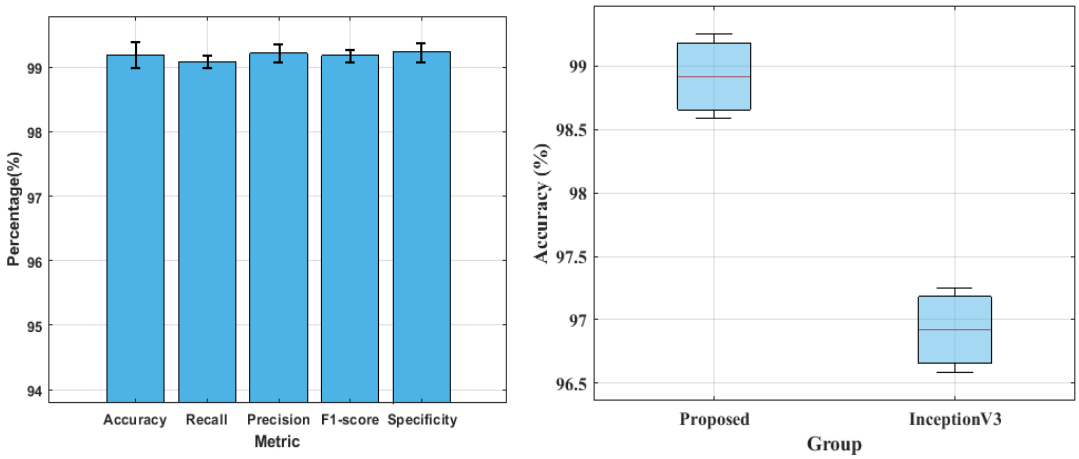

(a) (b)

Figure. 5 Statistical analysis of proposed method(a). CXR14 dataset(b). COVID-19 dataset

Table 5 illustrates computational complexity of proposed method with existing methods. The results representsthat the proposed HGSP-CNN achieves efficient computation with the lowest runtime memory and instance time compared to existing CNNs. The reduced parameter count and hypergraph-based feature fusion contribute to faster convergence and lower memory utilization. These characteristics make the model suitable for real-time medical applications without compromising accuracy.

Fig. 3 illustrates the confusion matrix of proposed method for pulmonary disease classification. Every cell in the matrix denotes number of correct and incorrect predictions, where the diagonal elements denote true positives accurately determined through an approach. In addition, to provide a detailed error characterization, per-class precision, recall and F1-score are reported for all the evaluated classes. The confusion matrices are included to visualize the class-wise misclassification patterns and to identify dominant error modes.

Particularly, this is done among visually overlapping pulmonary conditions. This analysis highlights the aggregate metrics by emphasizing class-specific strengths and weaknesses of proposed model. The high concentration of values along the diagonal indicates that the HGSP-CNN achieves excellent class discrimination, effectively reducing both false positives as well as negatives. The negligible off-diagonal elements demonstrate an approach's capacity to simplify well over datasets, reflecting its better recognition ability and consistency in detecting multiple lung abnormalities with minimal misclassification.

Fig. 4 represents the ROC of proposed method for pulmonary disease classification. A ROC curve is plotted against a number of thresholds and indicates an AUC. The ROC curve plots TPR over FPR at varying threshold values, providing a comprehensive measure of model's classification performance. The proposed model achieves ROC value close to 1 for both CXR14 and COVID-19 Radiography datasets, indicating near-perfect separability between the disease and normal classes.

Fig. 5 illustrates the statistical analysis of proposed method using CXR14 and COVID-19 datasets. A statistical evaluation using the independent t-test was conducted to determine whether the performance improvement of the proposed HGSP-CNN model over existing methods was statistically significant.

Table 6 represents the class-wise performance of proposed model evaluated using performance metrics from the confusion matric. These metrics provide a detailed assessment of the model discriminative capability for each class while highlighting its effectiveness in correctly identifying each case.

For the COVID-19 Radiography dataset, the mean classification accuracy of Group 1 (HGSP-CNN) was 98.92%, compared to 96.92% for Group 2 (baseline models).

Table 6. The class-wise results of proposed HGSP-CNN model for pulmonary disease classification

Class	Accuracy	Precision	Recall	F1-score
COVID	0.9976	0.9904	0.9959	0.9931
Lung-opacity	0.9974	0.9967	0.9942	0.9954
Normal	0.9972	0.9975	0.9966	0.9971
Viral Pneumonia	0.9983	0.9852	0.9888	0.9870

Table 7. Ablation Study of the proposed method for pulmonary disease classification

Dataset	Methods	Accuracy (%)	Precision (%)	Recall (%)	F1-score (%)	Specificity (%)
CXR14	CNN	96.72	96.10	95.88	95.99	96.25
	Standard HGNN	98.55	98.12	97.94	98.03	98.28
	CNN + Spiking neural P system	99.05	98.78	98.52	98.65	98.92
	Full CNN + HGSP (including preprocessing, fully connected layer)	99.58	99.26	99.17	99.34	99.68
COVID-19	CNN	97.86	96.42	96.81	97.13	97.25
	Standard HGNN	98.32	97.05	97.26	97.88	97.74
	CNN + Spiking neural P system	98.71	97.56	97.88	98.25	98.13
	Full CNN + HGSP (including preprocessing, fully connected layer)	99.25	98.23	98.43	99.37	99.21

Table 8. The performance impact of different hyperedge activation thresholds

Threshold Percentile	Avg. Hyperedges per Image	Accuracy (%)
50th percentile	12–15	98.41
65th percentile	8–11	99.02
75th percentile	4–9	99.58
85th percentile	3–6	99.11
90th percentile	1–4	98.64

Table 9. Comparative analysis of proposed method with state-of-art methods reported in literature review

Dataset	Methods	Accuracy (%)	Precision (%)	Recall (%)	F1-score (%)	Specificity (%)

CXR14	ViT-ASL [21]	73.21	32.19	76.75	42.60	72.21
	ResNet50-V2 [22]	93.4	54	55	54.4	98.5
	Proposed HGSP-CNN	99.58	99.26	99.17	99.34	99.68
COVID-19 Radiography	PulmoNet [25]	94	90.52	95.01	88.65	-
	F-RNN-LSTM with robust normalization [26]	95.04	93.65	96.78	95.19	94.21
	BSD [28]	95.76	95.76	95.76	95.75	-
	Proposed HGSP-CNN	99.25	98.23	98.43	99.37	99.21

The obtained t-statistic was 8.9772 with 6 degrees of freedom, resulting in a p-value of 0.0001, which is minimum to 0.05 significance level. This represents that the observed variation in mean accuracy among different sets is statistically important and unlikely due to random variation.To ensure robust and unbiased performance evaluation, a patient-stratified k-fold cross-validation protocol (k=5) was adopted. Here, all images from the same patient were assigned exclusively to a single fold. This strategy preserves sample independence and prevents information leakage between training and testing sets. In addition, to quantify uncertainty, 95% confidence intervals for accuracy are estimated using nonparametric bootstrap resampling with 1000 iterations across fold-level results. This mechanism does not assume normality and provides a robust estimation of performance variability. Additionally, the fold-wise standard deviation is reported to show the stability across different data partitions. It is observed from Fig. 5 that the fold-wise performance distribution of proposed model across CXR14 and COVID-19radiography datasets. The variance and consistent performance across folds indicates that stable learning behavior and robustness to data partitioning. This statistical analysis is presented to provide supportive evidence of consistency instead of definitive inferential guarantees. All these reported performance metrics are computed using fixed decision rules without ant post-hoc probability calibration. Similarly, for the CXR14 dataset, the mean accuracy for Group 1 was 99.36%, whereas Group 2 achieved 97.32%. The corresponding t-statistic was 19.6946 with 6 degrees of freedom and a p-value of 0.0003, again confirming a statistically significant improvement ($p < 0.05$). These outcomes substantiate that the proposed HGSP-CNN model provides a consistently improved classification performance across datasets, establishing the reliability and robustness of its predictive capability.

Table 7 demonstrates the ablation study of proposed method using different datasets. The integration of global pooling and graph connections yields moderate performance gains, whereas the introduction of hypergraph layers results in a substantial boost in accuracy and F1-score. This demonstrates that hypergraph reasoning becomes an important part in improving the discriminative capability of the model for complex pulmonary features.The results indicate that preprocessing contributes to improved feature clarity and improves the raw CNN baseline model by 0.82%. Then, the incorporation of hypergraph modeling further enhances performance by capturing high-order relational dependencies and contributes an additional 0.48% improvement. Finally, the integration of Spiking P System produces the largest incremental gain while demonstrating that spike-based thresholded propagation enhances the discriminative reasoning. Therefore, the performance improvement is achieved through cumulative integration which enhanced input quality, hypergraph modeling and spiking dynamics. To facilitate reproducibility and fair evaluation, all the model components are trained under identical preprocessing pipelines, data splits and optimization settings. The ablation study selectively disables the hypergraph modules and the SPS mechanism while maintaining comparable network capacity. Collectively, all these classification results are obtained using a fixed decision rule on maximum predicted class score without post-hoc threshold tuning. The same decision policy is introduced consistently across all the compared methods to ensure fairness. It is noted that no dataset-specific threshold optimization was performed.

Table 8 demonstrated consistently high performance across all the classes with strong performance by indicating robust classification capability. The slight variation in viral pneumonia reflects the minor inter-class confusion. Overall, these findings confirms that the proposed model achieves reliable and balanced performance for multi-class chest X-ray classification. Moreover, the 75th percentile activation threshold was selected to balance sparsity and representation in hyperedge construction. The lower thresholds include larger number of weakly activated nodes that resulted in overly dense hypergraphs and introduces redundant relational connections. The validation of this percentile activation is given in below Table 8.

The Table 8 represents the sensitivity analysis of different activation thresholds for hyperedge construction. When the threshold was reduced to 50th percentile, the hyperedge became densely connected which led to

redundant feature grouping and reduced accuracy. Increasing the threshold beyond 75th percentile resulted in sparse hypergraphs which limited relational reasoning.

4.2 Comparative Analysis

Table 9 illustrates the comparative analysis of proposed approach with existing methods based on different datasets. The existing methods such as ViT-ASL [21], ResNet50-V2 [22], PulmoNet [25], F-RNN-LSTM with robust normalization [26] and BSD [28] are estimated and compared with proposed method. In this research, the decimal values of existing methods named ViT-ASL [21] are changed into percentage based on the proposed method for better understanding. The comparison was conducted under different experimental settings including varying datasets, class definitions, labelling schemes, data splits and preprocessing pipelines. Therefore, the comparison is provided only as a contextual reference to provide performance trends of pulmonary disease classification instead a strict head-to-head benchmark. Direct superiority claims are avoided and the primary validation of proposed HGSP-CNN is based on controlled experiments conducted under identical experimental conditions within the work.

4.3 Discussion

The experimental analysis clearly indicates that the proposed HGSP-CNN framework provides substantial improvements over conventional CNN architectures. The integration of hypergraph topology enables high-order feature representation, allowing the network to capture inter-regional dependencies within the lung. The preprocessing pipeline enhances contrast and removes noise, ensuring more reliable input data for training. Comparative and ablation studies validate that hypergraph-based reasoning significantly contributes to classification accuracy. Additionally, the low computational complexity highlights its suitability for clinical environments requiring rapid diagnostics. The profiling procedure was conducted using a single forward pass at a fixed input resolution and batch size. FLOPS and parameter counts are reported to complement runtime measurements. The model achieves a fine balance between precision, recall, and specificity, which demonstrates its robustness against false detections. Even though, the COVID-19 radiography dataset provides verified COVID-18 annotations but contains a limited number of samples and class distributions that may not reflect real-world prevalence. To mitigate bias, a patient-level stratified splitting was employed to preserve class balance across evaluation sets. The failure analysis was conducted on misclassified samples from test data. It includes subtle opacities with low contrast were sometimes suppressed during preprocessing that led to insufficient hypervertex activation and fewehyperedges. Overall, the HGSP-CNN not only achieves improved quantitative results but also provides an interpretable and scalable solution for real-world pulmonary disease detection.

5. Conclusion

This research proposed an innovative HGSP-CNN for pulmonary disease classification using chest X-ray images. The model integrates advanced preprocessing, hypergraph learning, and spiking neuron dynamics to achieve enhanced interpretability and robustness. The integration of hypergraph reasoning significantly enhances the interpretability and scalability of the diagnostic framework. The proposed HGSP-CNN models complex inter-region dependencies through hierarchical hypergraph neurons, enabling better understanding of lung tissue structures and subtle pathological variations. From a clinical perspective, the proposed approach supports radiologists by providing rapid, accurate, and consistent diagnostic decisions, thereby reducing human error and interpretation variability. Its reduced computational complexity and high accuracy make it highly adaptable for integration into real-time healthcare systems, telemedicine platforms, and low-resource diagnostic centers. This capability substantially reduces diagnostic ambiguity between overlapping conditions such as pneumonia, tuberculosis, and COVID-19. Experimental results demonstrate significant improvements in accuracy, precision, and computational efficiency compared to existing CNN architectures. The integration of hypergraph reasoning enables deeper spatial understanding of pulmonary structures, while the optimized preprocessing ensures data consistency. The proposed framework offers a reliable, scalable, and computationally efficient solution for automated medical diagnostics and can be extended to other medical imaging domains in future research.

Notation list

Notations	Descriptions
$H(v, e)$	Incidence function
v and e	Hypervertex and hyperedge respectively
Π	Complete SPS approach

L	Set of rules that governs spiking, communication, and transformation of spike trains
syn	Synaptic connection structure
$\varphi = \{\alpha\}$	Group of spikes α
$\sigma_k = \{\sigma_v, \sigma_e, \sigma_u\}$	Group of neurons in HGSP
$k \in \{v, e, u\}$	Neuron classes
σ_v, σ_e and σ_u	Group of hypervertex, hyperedge and hyper-upper neurons individually
$\sigma_k = \{n_k, T_k, \omega_k, R_k\}$	The information of such hyper neurons
n_k	Primary number of spikes in σ_k
$T_k = \{\tau_{k,1}, \dots, T_{k,d}\}$	Spike train in σ_k
k, d	Length d of spike train T_k
ω_k	Weight of spike train
R_k	Finite group of guidelines through pursuing various forms
α^c	Number of spikes consumed
ω_{k_i} and $\omega_{k_{i+1}}$	Weight of the spike train currently present and next neuron k_i and k_{i+1} respectively
T_{k_i}	Spike train associated with neuronk_i
$T_{k_{i+1}}$	Updated spike train generated for the next neuron in the hierarchy or hyperedge connection
α^p	Number of spikes produced and sent to the next connected neuron after the rule fires
T_q	New spike train generated and transmitted to the next neuron q
q	Index of target neuron receiving the output spike train from neuron k
TP	True Positive
TN	True Negative
FP	False Positive
FN	False Negative

Conflicts of interest

The authors declare no conflict of interest.

Author contributions

Conceptualization, JSP and ST; methodology, JSP; software, ST; validation, JSP and ST; formal analysis, JSP; investigation, ST; resources, JSP; data curation, ST; writing—original draft preparation, JSP; writing—review and editing, ST; visualization, JSP; supervision, JSP; project administration, JSP; funding acquisition, ST.

Acknowledgments

The author sincerely thanks the Department of Electronics and Communication Engineering, Vardhaman College of Engineering, Hyderabad, for providing the necessary support to carry out this research. The author also acknowledges the guidance and encouragement received from the research supervisors at Dayananda Sagar College of Engineering, Bengaluru, under VisvesvarayaTechnological University (VTU), Belgaum. This research did not receive any specific grant from funding agencies in the public, commercial, or not-for-profit sectors.

References

1. R.D. Bhosale and D.M. Yadav, "Customized convolutional neural network for pulmonary multi-disease classification using chest x-ray images", *Multimedia Tools and Applications,* Vol. 83, No. 6, pp. 18537-18571, 2023.
2. S.U. Amin, S. Taj, A. Hussain, and S. Seo, "An automated chest X-ray analysis for COVID-19, tuberculosis, and pneumonia employingensemblelearningapproach", *Biomedical Signal Processing and Control*, Vol.87, p.105408, 2024.
3. T. Du Plessis,G. Ramkilawon, W.I.D. Rae, T. Botha, N.A. Martinson, S.A.P. Dixon, A. Kyme, and M.M. Sathekge, "Introducing a secondary segmentation to construct a radiomics model for pulmonary tuberculosis cavities", *La radiologiamedica*, Vol. 128, No. 9, pp. 1093-1102, 2023.
4. A. Kareem, H. Liu, and V. Velisavljevic, "A federated learning framework for pneumonia image detection using distributed data", *Healthcare Analytics*, Vol. 4, p. 100204, 2023.
5. A. Sulaiman, V. Anand, S. Gupta, Y. Asiri, M.A. Elmagzoub, M.S.A. Reshan, and A. Shaikh, "A convolutional neural network architecture for segmentation of lung diseases using chest X-ray images", *Diagnostics*, Vol. 13, No. 9, p.1651, 2023.
6. A.G. Argho, M.M.S. Maswood, M.I. Mahmood, and N. Mondol, "EfficientCovNet: A CNN-based approach to detect various pulmonary diseases including COVID-19 using modified EfficientNet", *Intelligent systems with applications*, Vol. 21, p. 200315, 2024.
7. R. Wang, L.C. Chen, L. Moukheiber, K.P. Seastedt, M. Moukheiber, D. Moukheiber, Z. Zaiman, S. Moukheiber, T. Litchman, H. Trivedi, and R. Steinberg, "Enabling chronic obstructive pulmonary disease diagnosis through chest X-rays: A multi-site and multi-modality study", *International Journal of Medical Informatics*, Vol. 178, p. 105211, 2023.
8. T. Geroski, O. Pavić, L. Dašić, D. Milovanović, M. Petrović, and N. Filipović, "SoftLungX: leveraging transfer learning with convolutional neural networks for accurate respiratory disease classification in chest X-ray images", *Journal of Big Data*, Vol. 11, No. 1, p. 146, 2024.
9. G.D. Deepak and S.K. Bhat, "A multi-stage deep learning approach for comprehensive lung disease classification from x-ray images", *Expert Systems with Applications*, Vol. 277, p. 127220, 2025.
10. S.H. Karaddi and L.D. Sharma, "Automated multi-class classification of lung diseases from CXR-images using pre-trained convolutional neural networks", *Expert Systems with Applications,* Vol. 211, p.118650, 2023.
11. M. Nahiduzzaman, M.O.F. Goni, R. Hassan, M.R. Islam, M.K. Syfullah, S.M. Shahriar, M.S. Anower, M. Ahsan, J. Haider, and M. Kowalski, "Parallel CNN-ELM: A multiclass classification of chest X-ray images to identify seventeen lung diseases including COVID-19", *Expert Systems with Applications*, Vol. 229, p. 120528, 2023.
12. A.U. Ibrahim, M. Ozsoz, S. Serte, F. Al-Turjman, and P.S. Yakoi, "Pneumonia classification using deep learning from chest X-ray images during COVID-19", *Cognitive computation*, Vol. 16, No. 4, pp. 1589-1601, 2021.
13. P. Patil and V. Narawade, "RESP dataset construction with multiclass classification in respiratory disease infection detection using machine learning approach", *International Journal of Information Technology*, 2024.
14. G. Mohan, M.M. Subashini, S. Balan, and S. Singh, "A multiclass deep learning algorithm for healthy lung, Covid-19 and pneumonia disease detection from chest X-ray images", *Discover Artificial Intelligence*, Vol. 4, No. 1, p.20, 2024.
15. Z. Liu, Y. Cheng, and S.Tamura, "Multi-label local to global learning: A novel learning paradigm for chest x-ray abnormality classification", *IEEE Journal of Biomedical and Health Informatics*, Vol. 27,No. 9, pp. 4409-4420, 2023.
16. R.D. Ishwerlal, R. Agarwal, and K.S. Sujatha, "Lungdisease classification using chest X ray image: An optimal ensemble of classification with hybrid training", *Biomedical Signal Processing and Control*, Vol. 91, p. 105941, 2024.
17. V. Ravi, V. Acharya, and M. Alazab, "A multichannel EfficientNet deep learning-based stacking ensemble approach for lung disease detection using chest X-ray images", *Cluster Computing*, Vol. 26, No. 2, pp. 1181-1203, 2022.
18. H. Malik, T. Anees, M. Din, and A. Naeem, "CDC_Net: Multi-classification convolutional neural network model for detection of COVID-19, pneumothorax, pneumonia, lung Cancer, and tuberculosis using chest X-rays", *Multimedia Tools and Applications*, Vol. 82, No. 9, pp. 13855-13880, 2022.
19. Y.H. Bhosale and K.S. Patnaik, "PulDi-COVID: Chronic obstructive pulmonary (lung) diseases with COVID-19 classification using ensemble deep convolutional neural network from chest X-ray images to minimize severity and mortality rates", *Biomedical Signal Processing and Control*, Vol. 81, p. 104445, 2023.
20. E. Mahamud, N. Fahad, M. Assaduzzaman, S.M. Zain, K.O.M. Goh, and M.K. Morol, "An explainable artificial intelligence model for multiple lung diseases classification from chest X-ray images using fine-tuned transfer learning", *Decision analytics journal*, Vol. 12, p.100499, 2024.
21. A. Mezinaand R. Burget, "Detection of post-COVID-19-related pulmonary diseases in X-ray images using Vision Transformer-based neural network", *Biomedical Signal Processing and Control*, Vol. 87, p. 105380, 2024.

22. M. Irtaza, A. Ali, M. Gulzar, and A. Wali, "Multi-label classification of lung diseases using deep learning", *IEEE Access*, Vol. 12, pp. 124062-124080, 2024.
23. F.J.M. Shamrat, S. Azam, A. Karim, K. Ahmed, F.M. Bui, and F. De Boer, "High-precision multiclass classification of lung disease through customized MobileNetV2 from chest X-ray images", *Computers in Biology and Medicine*, Vol. 155, p. 106646, 2023.
24. L.M.A. El-Magd, G.Dahy, T.A. Farrag, A. Darwish, and A.E. Hassnien, "An interpretable deep learning-based approach for chronic obstructive pulmonary disease using explainable artificial intelligence", *International Journal of Information Technology*, Vol. 17, No. 7, pp.4077-4092, 2024.
25. A.T. Abdulahi, R.O. Ogundokun, A.R. Adenike, M.A. Shah, and Y.K. Ahmed, "PulmoNet: a novel deep learning based pulmonary diseases detection model", *BMC Medical Imaging*, Vol. 24, No. 1, p. 51, 2024.
26. S. Goyal and R. Singh, "Detection and classification of lung diseases for pneumonia and Covid-19 using machine and deep learning techniques", *Journal of Ambient Intelligence and Humanized Computing*, Vol. 14, No. 4, pp. 3239-3259, 2021.
27. A. Bennour, N.B. Aoun, O.I. Khalaf, F. Ghabban, W.K. Wong, and S. Algburi, "Contribution to pulmonary diseases diagnostic from X-ray images using innovative deep learning models", *Heliyon*, Vol. 10, No. 9, p. e30308, 2024.
28. S. Yi, S. Qin, F. She, and D. Shao, "BSD: A multi-task framework for pulmonary disease classification using deep learning", *Expert Systems with Applications*, Vol. 259, p. 125355, 2025.
29. CXR14 dataset link: https://www.kaggle.com/datasets/nih-chest-xrays/data COVID-19. (Accessed on October 2025)
30. COVID-19 Radiography dataset link: https://www.kaggle.com/datasets/tawsifurrahman/covid19-radiography-database. (Accessed on October 2025)
31. M.A. Asham, A.A. Al-Shargabi, R. Al-Sabri, and I. Meftah, "A lightweight deep learning model with knowledge distillation for pulmonary diseases detection in chest X-rays", *Multimedia Tools and Applications*, Vol. 84, No. 15, pp. 14885-14913, 2024.
32. S. Shanthi, S. Saradha, J.A. Smitha, N. Prasath, and H. Anandakumar, "An efficient automatic brain tumor classification using optimized hybrid deep neural network", *International Journal of Intelligent Networks*, Vol. 3, pp. 188-196, 2022.